Design of High-Bandwidth Motor System Considering Electrical and Mechanical Time Constants

Soo-Hwan Park, Jin-Cheol Park, Ho-Young Lee, Soon-O Kwon, and Myung-Seop Lim, *Member, IEEE*

***Abstract*—This article proposes a design method for a high-speed response motor system consisting of a motor and load. Various methods have been studied to improve the speed response of the motor system, but the main focus was previously advanced control techniques. However, the dynamic response of the controller can be further improved with the high-speed response motor system. The proposed method improves the speed response by increasing the bandwidth of the motor system, which is the plant of the servo system. Thus, the relationship between the bandwidth, which is an indicator of speed response and the motor system, is investigated. The motor system consists of the electrical and mechanical parameters. As both electrical and mechanical parameters affect the speed response and bandwidth of the motor system, the correlation of the time constants and bandwidth is analyzed. Based on the analyzed results, the process of designing a motor system with maximized bandwidth is introduced. An experimental based friction model is proposed to estimate the accurate speed responses and required torque of the motor system. Therefore, a motor system with maximized bandwidth is designed using the proposed design process and friction model. Finally, the rated power and speed response of the motor system are verified through simulations and experiments.**

***Index Terms*—Bandwidth, electrical time constant, friction modeling, mechanical time constant, speed response, surface-mounted permanent magnet synchronous motor (SPMSM).**

I. Introduction

MOTOR system is controlled by feedback such as torque, speed, and position feedback. The purpose of controlling the motor system is to obtain the desired response within the desired time. In particular, the speed response of the motor system affects the position response and greatly depends on the design results. It is, therefore, important to improve the speed response of the motor system. A typical method for improving the response is to change the control techniques. However, the dynamic response of the controller can be further improved when the dynamic response of the plant improves [1].

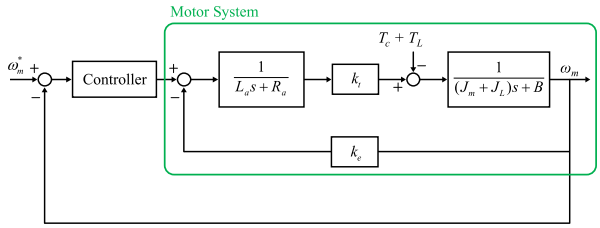

Fig. 1. Configuration of the servo system.

A permanent magnet synchronous motor (PMSM) is mainly used with reducers rather than direct drive [2]. The PMSM is classified into the surface-mounted PMSM (SPMSM) and interior PMSM (IPMSM) according to the rotor type [3]. For precision motion control, the SPMSM, which has a small torque ripple, is appropriate. Therefore, the motor system for precision motion control consists of the motor drive, SPMSM, and reducer.

Many control techniques have been proposed to improve the speed response [4], [5]. As a real-time performance of the digital signal processor has been improved, the control techniques using spare computing power have been proposed [6]–[8]. Yoo *et al.* proposed a method to improve the bandwidth of the current regulator by reducing the digital execution delay [6]. Idkhajine *et al.* improves execution time to calculate complex sensorless controls by applying field-programmable gate arrays [7]. As the bandwidth of the current regulator increases, the research has attempted to solve various problems in the motor system [8], [9]. Researchers have studied several compensation algorithms to improve the characteristics of switching devices such as dead-time and the rising and falling delays of IGBT [10]–[12]. Several studies have been carried out to improve the performance of the current regulator by modeling and compensating measurement errors of currents due to digital control [13], [14].

A complete servo system consists of a controller and plant. Since the motor system is a plant of the servo system as shown in Fig. 1, the motor system is accompanied by disturbances and often maintain their current position, speed, or torque in

Manuscript received December 30, 2019; revised April 1, 2020; accepted May 15, 2020. Date of publication May 29, 2020; date of current version September 18, 2020. Paper 2019-EMC-1539.R1, presented at the 2019 IEEE Energy Conversion Congress and Exposition, Baltimore, MD, USA, Sep. 29.Oct. 3, and approved for publication in the IEEE TRANSACTIONS ON INDUSTRY APPLICATIONS by the Electric Machines Committee of the IEEE Industry Applications Society. This work was supported by the National Research Foundation of Korea funded by the Korea government (Ministry of Science, ICT & Future Planning) under Grant 2018R1C1B5085447. *(Corresponding author: Myung-Seop Lim.)*

Soo-Hwan Park, Jin-Cheol Park, and Myung-Seop Lim are with Hanyang University, Seoul 04763, South Korea (e-mail: shwanp14@hanyang.ac.kr; skensk1990@hanyang.ac.kr; myungseop@hanyang.ac.kr).

Ho-Young Lee is with Hanyang University, Seoul 04763, South Korea, and also with the Korea Institute of Industrial Technology, Daegu 42994, South Korea (e-mail: cyber5385@kitech.re.kr).

Soon-O Kwon is with the Korea Institute of Industrial Technology, Daegu 42994, South Korea (e-mail: kso1975@kitech.re.kr).

Color versions of one or more of the figures in this article are available online at https://ieeexplore.ieee.org.

Digital Object Identifier 10.1109/TIA.2020.2998674

the event of disturbance. Therefore, it is important to increase the bandwidth of motor system in order to respond with the sudden disturbances. Most studies about dynamic response are concentrated on the controller shown as aforementioned references. The ultimate improvement of the response should be accompanied by appropriate control techniques and increasing the bandwidth of the motor system. Despite the importance of the motor system bandwidth, little research has been conducted on the bandwidth of the motor system. Lim *et al.* studied motor design to improve the speed response in high-speed machine application [15]. However, since the actual friction model was not considered, accurate prediction of the speed response was difficult. Kim *et al.* predicted speed response using an electromechanical time constant, but since the viscous friction coefficient was not considered, an electromechanical time constant was used only as a simple index to compare the speed response [16].

This article proposes a design method for improving the speed response of the motor system considering electrical and mechanical time constants. An SPMSM for a high-bandwidth motor system was designed and the speed response was verified through simulations and experiments.

In this study, the bandwidth of motor system is introduced to evaluate the speed response of the motor system. As the bandwidth consisted of electrical and mechanical time constants, the relationship between the time constants and the design variables, such as rotor size and series turns per phase, are analyzed. The electrical parameters, consisting of the resistance, inductance, and the back electromotive force (back EMF), determine the electromagnetic performance and current response the same as the torque response. The mechanical parameters consisting of the moment of inertia, Coulomb friction torque, and viscous friction coefficient determine the friction torque and speed response. These electrical and mechanical parameters vary with pole and slot combinations, rotor size, series turns per phase, and core geometry. As the bandwidth depends on both the electrical and mechanical parameters, the relationship between the time constants and bandwidth must be analyzed in order to maximize the speed response of the motor system.

This article is organized as follows. The relationship between the speed response and bandwidth was investigated in Section II. Then, the correlation of the bandwidth and electrical and mechanical time constants was discussed in Section III. In Section IV, the friction model based on the experiments was proposed in order for the accurate simulation to analyze the speed response. Finally, the SPMSM for a high-bandwidth motor system was designed with experimental verification.

II. Speed Response of the Motor System

A. Transfer Function of the Motor System

The motor system is composed of an electromagnetic system and mechanical system. The two systems are integrated via the motor torque. Since the electromagnetic system uses a three-phase brushless motor, a phase voltage can be expressed as

$$V_a = R_a i_a + L_a \frac{di_a}{dt} + e_a = R_a i_a + L_a \frac{di_a}{dt} + k_e \omega_m \tag{1}$$

where V_a, i_a, and e_a are phase voltage, armature current, and the back EMF per phase; R_a and L_a are armature resistance and inductance per phase, respectively, and k_e and ω_m are the back EMF constant and the mechanical speed, respectively. The mechanical system is expressed by the equation of motion as follows:

$$T_e = (J_m + J_L)\frac{d\omega_m}{dt} + B\omega_m + k\int \omega_m + T_c + T_L = k_t i_a \tag{2}$$

where T_e, T_c, and T_L are motor torque, Coulomb friction torque, and load torque, respectively; J_m and J_L are the inertia of the motor and load, respectively; B, k, and k_t are the viscous friction coefficient, spring constant, and torque constant of the motor, respectively. Since the load system that is used in this study consists of the gearbox, it is hard to expect the effect of dynamics in spring. Therefore, the spring constant is ignored in this study.

The integrated model of the system can be derived from the Laplace transformed equations of (1) and (2). The voltage equation in the Laplace domain is expressed as

$$V_a(s) = (R_a + sL_a)\, i_a(s) + k_e \omega_m(s). \tag{3}$$

The equation of motion in the Laplace domain is expressed as

$$k_t i_a(s) = \{s\,(J_m + J_L) + B\}\,\omega_m(s) + T_c(s) + T_L(s). \tag{4}$$

Based on (3) and (4), the integrated motor system is represented as Fig. 1. The motor torque, which is an output of the electromagnetic system, acts as the input of the mechanical system. The speed, which is the output of the mechanical system, is converted into back EMF and acts as feedback of the electromagnetic system. Then, the mechanical speed is obtained as

$$\omega_m(s) = \frac{k_t V_a - (L_a s + R_a)\,(T_L + T_c)}{(L_a s + R_a)\,\{s\,(J_m + J_L) + B\} + k_e k_t}. \tag{5}$$

In (5), the load torque and Coulomb friction torque, acting as disturbances in the mechanical system, affect the steady-state speed and do not affect the transient response [17]. Therefore, the disturbances are ignored to simplify the system to a single-input single-output (SISO) system. The simplified SISO system can be organized in a second-order standard transfer function as

$$\frac{\omega_m}{V_a} = \frac{k_t}{k_e k_t + R_a B}\frac{\omega_n^2}{s^2 + 2\zeta\omega_n s + \omega_n^2} \tag{6}$$

where

$$\omega_n = \sqrt{\frac{k_e k_t + R_a B}{(J_m + J_L)\,L_a}} = \sqrt{\frac{k_e k_t}{(J_m + J_L)\,L_a} + \frac{1}{\tau_e \tau_m}} \tag{7}$$

$$\zeta = \frac{(J_m + J_L)\,R_a + L_a B}{2\sqrt{L_a\,(J_m + J_L)\,(k_e k_t + R_a B)}} = \frac{\tau_e + \tau_m}{2\tau_e\tau_m\sqrt{\dfrac{k_e k_t}{(J_m + J_L)\,L_a} + \dfrac{1}{\tau_e\tau_m}}} \tag{8}$$

where

$$\tau_e = \frac{L_a}{R_a}, \quad \tau_m = \frac{J_m + J_L}{B}. \tag{9}$$

In the preceding equations, ω_n and ζ are the natural frequency and damping ratio of the motor system, respectively; τ_e and τ_m are the electrical and mechanical time constants, respectively.

B. Bandwidth and Speed Response

A high bandwidth means that the speed response can respond even at high-frequency bands, which are accompanied by rapidly varying disturbances. Therefore, it is necessary to increase the bandwidth so as to improve the speed response. The bandwidth ω_B is defined as the frequency range where the magnitude of the closed-loop gain does not drop below -3 dB expressed as

$$|G(j\omega_B)| = \frac{1}{\sqrt{2}},$$
$$\omega_B = \omega_n \left\{ \left(1 - 2\zeta^2\right) + \sqrt{4\zeta^4 - 4\zeta^2 + 2} \right\}^{\frac{1}{2}} \tag{10}$$

where $|G(j\omega)|$ is the gain of the closed-loop frequency response of the motor system. As shown in (10), the high natural frequency and low damping ratio are required to increase the bandwidth. However, the natural frequency and damping ratio have a trade-off relationship according to the electrical and mechanical time constants. Therefore, in order to design the high-bandwidth motor system, it is necessary to investigate the appropriate electrical and mechanical time constants.

III. Correlation Between the Bandwidth and Time Constants

A rotor size is determined by the rotor diameter and stack length. Hence, the rotor size affects both the reluctance of the air gap and the ratio of the stack length and rotor diameter. Therefore, the electrical and mechanical time constants are affected by changing the rotor size. As the flux linkage and wire diameter vary with the change of the series turns per phase, it affects the electrical parameters such as the resistance, inductance, and the back EMF constant. Therefore, the rotor diameter, stack length, and the series turns per phase should be determined considering the rated power and the high-speed response.

A. Electrical Time Constants

Fig. 2(a)–(d) shows the model of the equivalent magnetic circuit for a single pole and single coil. The magnetic circuit for single pole is used for calculating the back EMF, and the magnetic circuit for single coil is used for calculating the inductance. Fig. 2(a) shows a flux line under no-load condition, and the corresponding magnetic circuit is shown in Fig. 2(b). Since the back EMF is related to the flux due to the permanent magnet (PM), the magnetic circuit is composed of the reluctances of the core and PM. It is assumed that the iron core of the stator and the rotor have infinite permeability while the magnetic potential for each core is the same. The air-gap flux due to PM is represented

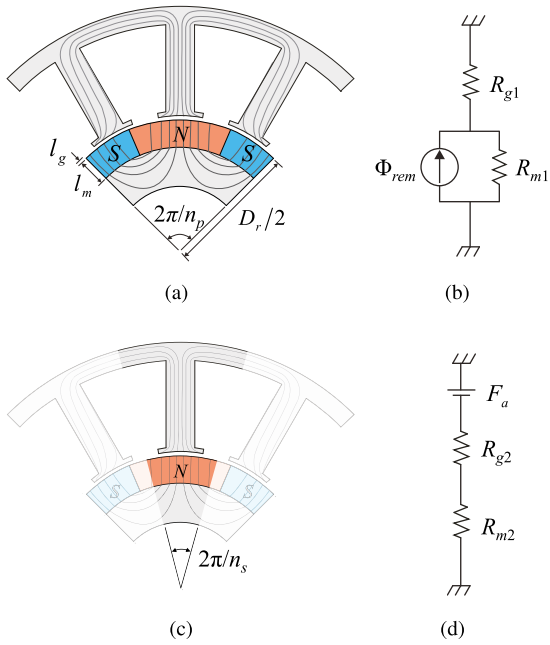

Fig. 2. Magnetic circuits of 8P12S. (a) No-load flux lines by PM and (b) corresponding equivalent magnetic circuit for single pole. (c) Flux lines by armature current only and (d) corresponding equivalent magnetic circuit for single coil.

as

$$\Phi_{gm} = \Phi_{rem} \frac{R_{m1}}{R_{m1} + R_{g1}} \tag{11}$$

where Φ_{gm} and Φ_{rem} are the air-gap flux and flux of PM; R_{m1} and R_{g1} are the reluctances of PM and air gap for single pole, respectively. The reluctance of PM for single pole is

$$R_{m1} = \frac{2n_p l_m}{\mu_0 \mu_{\text{rec}} \pi D_r L_{stk}} \tag{12}$$

where n_p is the pole pair, l_m is the length of PM; μ_0 and μ_{rec} are the air permeability and recoil permeability, respectively. The reluctance of air gap for single pole is as follows:

$$R_{g1} = \frac{2n_p l_g}{\mu_0 \pi D_r L_{stk}} \tag{13}$$

where l_g is the length of air gap. The air-gap flux that is computed from (11) to (13) is given by

$$\Phi_{gm} = \Phi_{rem} \frac{l_m}{l_m + \mu_{\text{rec}} l_g} \tag{14}$$

and the air-gap flux density is calculated by dividing the air-gap cross-sectional area

$$B_{gm} = B_{rem} \frac{l_m}{l_m + \mu_{\text{rec}} l_g} \tag{15}$$

where B_{gm} and B_{rem} are the flux density of air gap and PM, respectively. The back EMF is affected by the winding factor, series turns per phase, rotor size, and the air-gap flux density as

$$e_a = \omega_m k_{w1} N_{\text{ph}} D_r L_{stk} B_{gm} \tag{16}$$

where k_{w1} is the winding factor of fundamental harmonic; N_{ph} is the series turns per phase. Then, the back EMF is obtained by substituting (15) into (16) as

$$e_a = \frac{l_m}{l_m + \mu_{\text{rec}} l_g} \omega_m k_{w1} N_{\text{ph}} B_{rem} D_r L_{stk}. \tag{17}$$

Since the inductance is related to the flux due to the armature current, the flux line due to the armature current is shown as Fig. 2(c). The corresponding magnetic circuit is composed of the reluctances of the air gap and PM as Fig. 2(d). As the magnetic flux of 8P12S is divided in half by the neighboring tooth, mutual inductance is half of the self-inductance [24]. The phase inductance is also equal to the series connection of the inductance for a single coil. Then, the phase inductance is given by

$$L_a = \frac{n_s}{m}(L_s - L_m) \tag{18}$$

where

$$L_s = \left(\frac{N_{\text{ph}}}{n_s/m}\right)^2 \frac{1}{2\,(R_{m2} + R_{g2})} \tag{19}$$

where L_s and L_m are the self- and mutual inductances, respectively; n_s and m are the number of slots and phases, respectively; R_{m2} and R_{g2} are the reluctances of the PM and air gap for single coil, respectively. The reluctances of the air gap and PM for single coil are given by

$$R_{m2} = \frac{n_s l_m}{\mu_0 \mu_{\text{rec}} \pi D_r L_{stk}} \tag{20}$$

$$R_{g2} = \frac{n_s l_g}{\mu_0 \pi D_r L_{stk}}. \tag{21}$$

The resistance of the armature winding depends on the length of the conductor and wire diameter. The coil wound on the stator is divided into two parts of coil-side and end-coil. The end-coil is the conductor passing from one slot to another and the length of the end-coil is related to the size of the motor and the pole and slot combinations. The armature windings of 8P12S are wound with concentrated winding as shown in Fig. 3. Since the wire diameter with the highest fill factor is used, the resistance is calculated as

$$R_a = \rho_c \frac{4}{\pi} \frac{2\,(L_{stk} + l_{\text{end}})\, N_{\text{ph}}}{d^2} \{1 + \alpha\,(T - 20\,^\circ\text{C})\} \tag{22}$$

where

$$l_{\text{end}} = l_A + 2l_B \tag{23}$$

where ρ_c is the resistivity of copper; l_{end} and d are the end-coil length and wire diameter, respectively; α and T are the temperature coefficient of copper and temperature, respectively; l_A and l_B are the averaged coil span and height of the end-turn, respectively, as shown in Fig. 3. The armature current is limited by the current density because it acts as a heat source of the motor, increasing the coil temperature and resistance. When the flux generated by the PM is constant, the maximum torque is determined by the maximum armature current. Therefore, increasing the wire diameter while maintaining the current density is advantageous in increasing the armature current. However, due to the limited slot area, it is necessary to maintain a constant fill factor and to set the maximum wire diameter. When the fill factor and slot area are constant, the wire diameter is expressed as

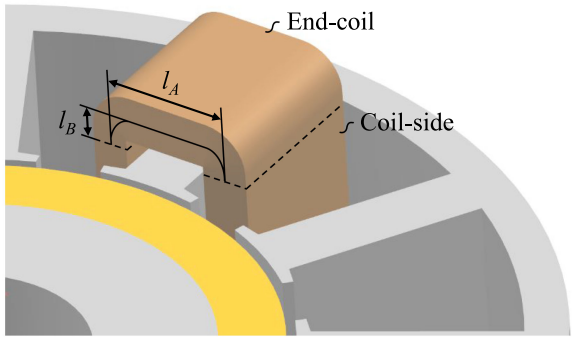

Fig. 3. Simplified armature coils of concentrated winding.

$$d = \sqrt{\frac{4}{\pi} \frac{(n_s/m) \cdot \text{Fill factor} \cdot A_{\text{slot}}}{N_{\text{ph}}}} \tag{24}$$

where

$$\text{Fill factor} = \frac{\pi}{4} \frac{N_{\text{ph}}}{(n_s/m)} \frac{d^2}{A_{\text{slot}}} \tag{25}$$

where A_{slot} is the slot area. The resistance is obtained by substituting (24) and (25), into (22) as

$$R_a = \frac{2\rho_c N_{\text{ph}}^2\,(L_{stk} + l_{\text{end}})}{(n_s/m) \cdot \text{Fill factor} \cdot A_{\text{slot}}} \{1 + \alpha\,(T - 20^\circ\text{C})\}. \tag{26}$$

Since both the resistance and inductance are proportional to the square of series turns per phase, the electrical time constant defined as the inductance to resistance is independent of the series turns per phase as

$$\tau_e = \frac{0.375\pi\mu_0\mu_{\text{rec}}\,(m/n_s)\,D_r L_{stk} \cdot \text{Fill factor} \cdot A_{\text{slot}}}{\rho_c\,(l_m + \mu_{\text{rec}} l_g)\,(L_{stk} + l_{\text{end}})\,\{1 + \alpha\,(T - 20^\circ\text{C})\}}. \tag{27}$$

B. Mechanical Time Constant

The shape of the rotor for calculating the rotor inertia can be simplified as shown in Fig. 4(a). It is assumed that the mass density of the PM and the iron core are the same. Then, the inertia of the rotor is as follows:

$$J_m = \frac{\pi}{32} \rho_r D_r^4 L_{stk} \tag{28}$$

where ρ_r is the equivalent mass density of rotor. Therefore, the mechanical time constant is independent of the series turns per

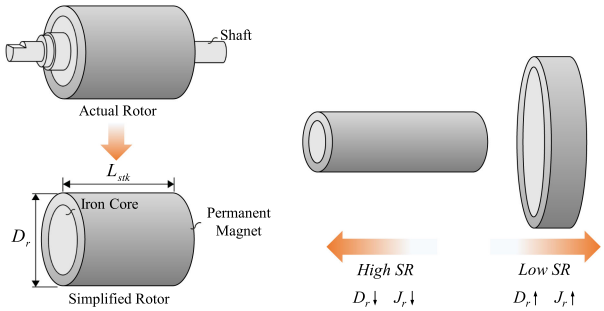

Fig. 4. Rotor inertia according to the rotor shape. (a) Simplified rotor shape. (b) Relationship between the SR and rotor inertia.

phase as well as the electrical time constant as

$$\tau_m = \frac{\frac{\pi}{32}\rho_r D_r^4 L_{stk} + J_L}{B}. \tag{29}$$

Finally, the bandwidth that is fully dependent on the rotor size is obtained by substituting (27) and (29) into (10). The studies in [15] and [16] used natural frequency and damping ratio as an index to evaluate the speed response. However, the indexes have a tradeoff relationship according to the design variables, such as rotor diameter, stack length, and fill factor. Thus, it is necessary to investigate the speed response according to the design variables. In this article, the speed response is analyzed by integrating the natural frequency and damping ratio according to the design variables. The designer can predict the speed response of the motor system and design appropriate controller using the bandwidth.

This article employs a torque per rotor volume (TRV), and a shape ratio (SR) to determine the rotor size. The TRV is defined as a rated torque per rotor volume and SR is defined as the ratio of the stack length and rotor diameter [16]. If the rotor volume is constant, the rotor inertia varies with the SR, as shown in Fig. 4(b). Therefore, the rotor size can be determined by searching for TRV and SR, which have the maximum bandwidth.

IV. Design and Verification

Fig. 5 shows the process of designing a motor that maximizes the bandwidth of the motor system. First, the experimental based friction model is proposed to determine the rated torque of the motor system and to predict the accurate speed response. The rated torque is calculated from the friction model and the motor should be able to be continuously driven at the rated torque. Then, the volume of the rotor is determined from the rated torque and TRV. As maintaining the back EMF is important to produce desired electromagnetic torque within limited voltage input, the series turns per phase can be determined according to the SR. After determining the wire diameter considering fill factor, the electrical and mechanical parameters can be calculated according to the SR. The bandwidth is calculated by using the evaluated parameters, and the design of the motor system with the maximum speed response is completed by selecting

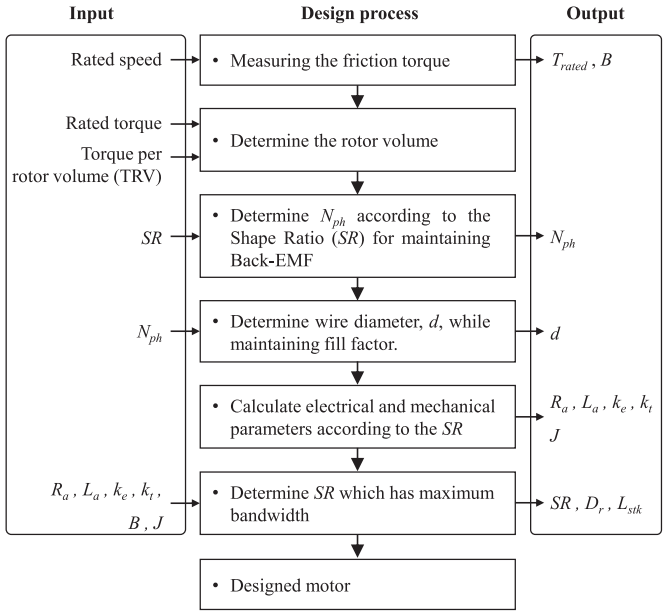

Fig. 5. Design process of a high-bandwidth motor.

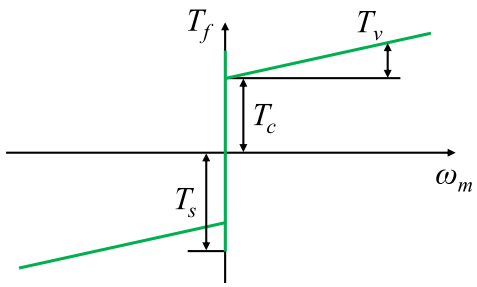

Fig. 6. Friction model consisting of static, Coulomb, and viscous friction torque.

the motor with largest bandwidth. The constraints are the stator outer diameter, stack length, rated power, and dc-link voltage. As the motor uses the ferrite magnet and is totally-enclosed, the TRV was set to 6.8 kN·m/m^3 with reference to the work in [3].

A. Experimental Based Friction Model

The presented motor system is used for the conveyor drive system. Since the system consists of motor, gearbox, and timing belt, there are many factors that generate friction. The rated torque is defined as a required torque for continuous drive without any load on the conveyor. Thus, the rated torque is equal to the friction torque at rated speed. However, as the required maximum torque of the motor system is defined as the sum of friction torque and load torque, the maximum torque of the motor should be determined in consideration of load torque.

For calculating the required torque of the motor system and simulating the speed response, the friction torque of (2) should be analyzed. The friction model, which is used in this article, consists of three frictional components, such as static friction, Coulomb friction, and viscous friction, as shown in Fig. 6.

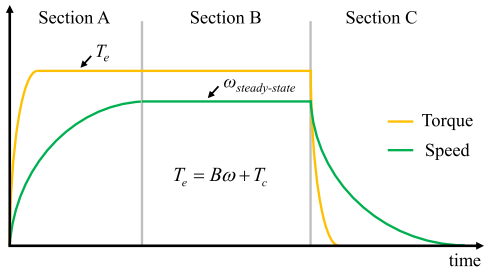

Fig. 7. Speed response of the rotating machinery.

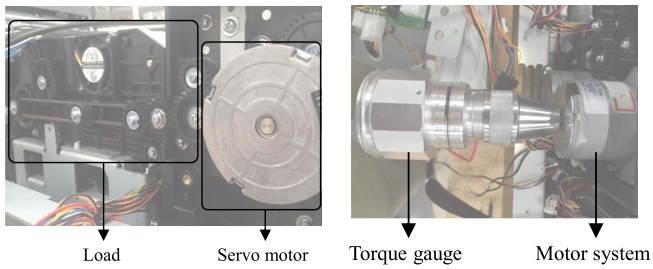

Fig. 8. Experiment sets for friction modeling. (a) Experiment set to measure the friction torque and (b) the starting torque.

Since the static friction occurs when the rotating machinery is stationary, the static friction torque has a maximum value when the rotor tries to move, and the friction torque is defined as the starting friction torque. When the rotating machinery rotates, the friction torque consists of Coulomb and viscous friction torque. Then, the friction model can be expressed as

$$T_f = \begin{cases} T_c \cdot \text{sgn}(\omega_m) + B\omega_m, & \text{if} \quad \omega_m \neq 0 \\ T_e, & \text{if} \quad \omega_m = 0\ ,\ |T_e| < T_s \\ T_s \cdot \text{sgn}(T_e), & \text{if} \quad \omega_m = 0\ ,\ |T_e| \geq T_s \end{cases} \tag{30}$$

where T_f, T_s, T_c, and T_e are the friction, starting, Coulomb friction torque, and electromagnetic torque, respectively; B and ω_m are the viscous friction coefficient and rotating speed of the motor, respectively. Since the friction torque is influenced by various conditions, such as tolerance and assembly conditions, it is difficult to predict analytically. Thus, it should be measured through the experiments.

Fig. 7 shows the speed response of the rotating machinery. Section A is the transient speed response when the step torque is applied. As the step torque input is same as the step current reference, the rise of the armature current is affected by the electrical time constant. Thus, the speed response is related to both the electrical and mechanical time constant.

As the speed increases, the friction torque also increases because of the viscous friction torque. When the input torque is equal to the friction torque, the rotating machinery enters a steady state, as shown in Section B. Therefore, the friction torque at a constant steady-state speed is equal to the input torque.

Section C shows the speed response when the current reference is set to zero. When the current reference is set to zero, all the switches are opened. The rate of decrease in current is affected by the electrical time constant. Then, the input torque is decreased also, and the speed decreases when the input torque is less than the friction torque. Since the decrease in speed is affected by the mechanical time constant, the speed response in Section C is also affected by the electrical and mechanical time constant.

The starting torque can be obtained by measuring the torque when the rotor starts to move, and the Coulomb and viscous friction torques can be obtained by fitting the friction torque according to the steady-state rotating speed. Since the Coulomb and viscous friction torques are calculated using the electromagnetic torque and steady-state speed, the accuracy of the friction model is determined according to the accuracy of the electromagnetic torque. Since the electromagnetic torque is proportional to the q-axis magnetizing current when the d-axis current is controlled to be zero, the electromagnetic torque can be expressed as

$$T_e = 1.5\ n_p\ \psi_a i_{oq} \tag{31}$$

where ψ_a is the flux linkage and i_{oq} is the q-axis magnetizing current. However, the measured q-axis current includes iron loss current when the eddy current loss of magnets is ignored [19]. The iron loss current can be obtained from the iron loss, which is calculated by the electromagnetic finite-element analysis (FEA). Then, the sum of Coulomb and viscous friction torque is equal to the electromagnetic torque when the rotating speed is in the steady state. As the electromagnetic torque can be calculated by using the magnetizing current excluding the iron loss current from the measured q-axis current, the friction torque can be expressed as

$$T_f = 1.5\ n_p\ \psi_a\ (i_q - i_{cq}) \tag{32}$$

where i_q is the measured q-axis current and i_{cq} is the q-axis iron loss current. Consequently, the friction model can be obtained by fitting linearly the friction torque according to the steady-state speed.

The experiment set for measuring the friction torque is shown in Fig. 8(a). A servomotor was coupled to the load to drive the load at a constant speed. When the servomotor operates the load, the friction torque at the steady-state speed can be measured with the q-axis current and torque constant of the servomotor. The torque constant of the servomotor is known from the datasheet. To measure the starting torque, a torque gauge is attached to the shaft connected to the motor, as shown in Fig. 8(b). The motor system starts to move when a torque greater than the starting torque is applied to the motor system. Therefore, the starting torque can be measured by measuring the torque when the motor system moves with the torque gauge.

Fig. 9 shows the result of measuring the friction torque in Section B of Fig. 7. Since the friction torque is proportional to the speed, the slope of the friction torque is equal to the viscous friction coefficient B, whereas the torque at the zero speed is equal to the coulomb friction torque T_c of the motor system. Then, the rated torque can be obtained from the friction torque

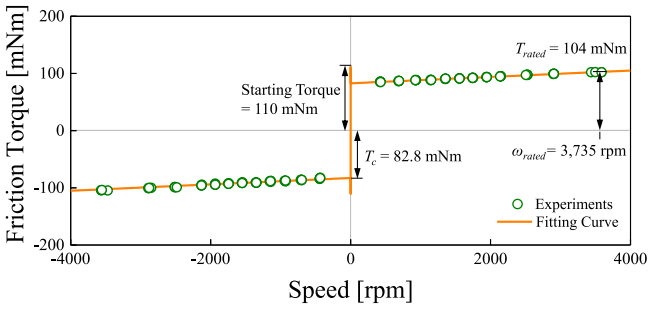

Fig. 9. Experimental results of measuring the friction torque of the load.

TABLE I
MOTOR SYSTEM SPECIFICATIONS

Item	Unit	Value
Poles / Slots	-	8 / 12
Stator outer diameter	mm	54
Stack length	mm	< 24
Rated power	W	40.7
Rated speed	rpm	3,735
Rated torque	mNm	104
Starting torque	mNm	110
Load torque	mNm	80
Load inertia	kg·m^2	3.05×10^{-5}
Viscous friction torque	mNm/rpm	0.00558
Coulomb friction torque	mNm	82.8
Current vector control	-	$i_d = 0$

at rated speed $\omega_{\rm rated}$ of 3735 r/min. The measurement results of starting torque are shown in Fig. 9 at zero speed.

As a result, the rated torque was measured as 104 mN·m, and the starting torque was measured as 110 mN·m. The specifications of the motor system are shown in Table I. The motor to be designed is 8P12S and the stator outer diameter is 54 mm. The rated torque and speed are 104 mN·m and 3735 r/min, respectively, whereas the rated power is 40.7 W. The inertia of load is 3.05×10^{-5} kg·m^2 and the viscous friction coefficient and the coulomb friction torque are 0.00558 mN·m/(r/min) and 82.8 mN·m, respectively. In addition, the maximum torque of the motor must be greater than the sum of starting torque and load torque of 190 mN·m. Since the only magnetic torque is generated by the *q-axis* current in SPMSM, the current vector control method of "$i_d = 0$" is used to investigate the speed response under the same conditions.

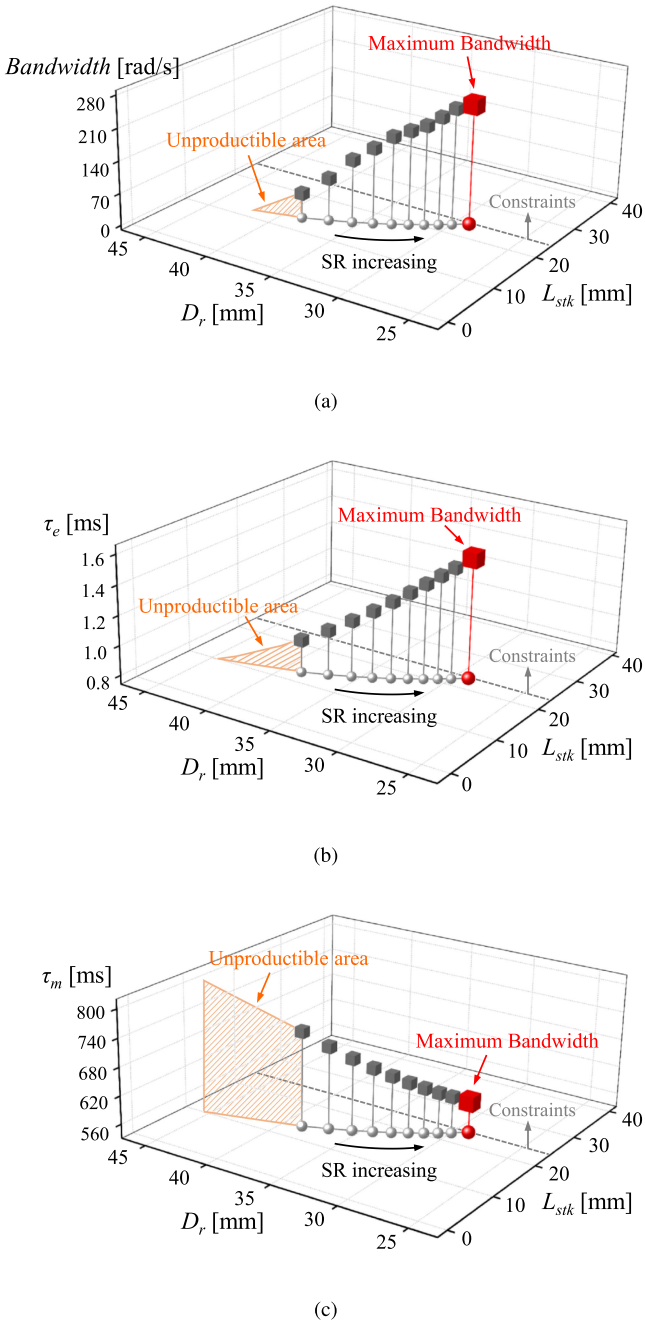

Fig. 10. Rotor sizing results to maximize the bandwidth. (a) Bandwidth. (b) Electrical time constant. (c) Mechanical time constant according to the shape ratio.

B. Design of Rotor and Stator

Since the rated torque is determined, the rotor volume can be determined using TRV. Then, the series turns per phase can be determined according to the SR for maintaining back EMF. Fig. 10(a)–(c) shows the calculation results of the bandwidth, electrical and mechanical time constants according to SR within limited conditions, such as stator outer diameter, stack length, and limited voltage. When determining the motor dimensions, the tooth and yoke width must be guaranteed to have a minimum value for manufacturing, so that the unproductible area may occur as the SR decreases. As the stator outer diameter is limited, the electrical parameters such as inductance and back EMF are affected by the magnetic saturation as the SR decreases. Thus, the electrical parameters should be calculated by using electromagnetic FEA.

As shown in Fig. 10(a), the high bandwidth can be achieved by increasing the SR. As the SR increases, the inductance is proportional to the product of rotor diameter and stack length, and the resistance changes nonlinear by the length of the end-turn. Thus, the electrical time constant is increased and the mechanical time

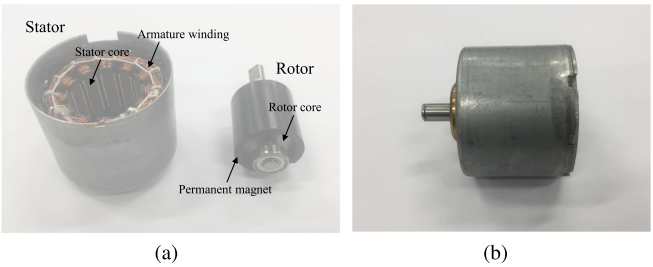

Fig. 11. Designed motor. (a) Stator and rotor. (b) Assembly of the designed motor.

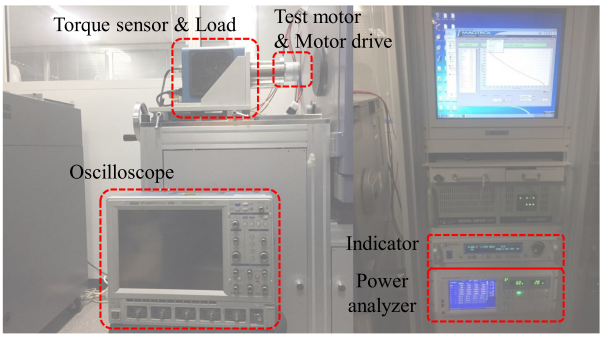

Fig. 12. Experimental setup to test the performance of the motor.

constant is decreased because the rotor inertia becomes smaller as SR increases. The change in time constants according to SR can be seen in Fig. 10(b) and (c). Then, the maximum bandwidth and SR are 252.4 rad/s and 0.82, respectively, considering the constraints.

After the rotor size is determined, the stator should be designed considering the magnetic circuit. Since the stator is magnetically saturated by the flux due to the PM and armature current, the width of the tooth and yoke should be determined so as to minimize the reluctance. The design process in [18], which is a method to minimize the reluctance of stator, is applied in this article. The flux through the tooth is divided into half along the yoke. The divided flux passes over the yoke to the next tooth. Then, the reluctance of the stator is determined along the magnetic flux path, and the tooth and yoke width are determined to generate the maximum flux when the armature current is the same.

C. Experimental Verification

Fig. 11 shows the stator, rotor, and assembly of the designed motor. The most effective way to verify the design results is to compare the designed motor with the other motor that has low bandwidth. Instead of comparing the designed motor with the other model, we focused on comparing the experimental results with the simulation results of the designed motor. To verify the validity of the design results, the electromagnetic performance at the rated power and the speed response to reach the rated power are verified. The torque, speed, and current characteristics of the motor were tested to verify the design results. The test was conducted using a dynamometer shown in Fig. 12. A Magtrol

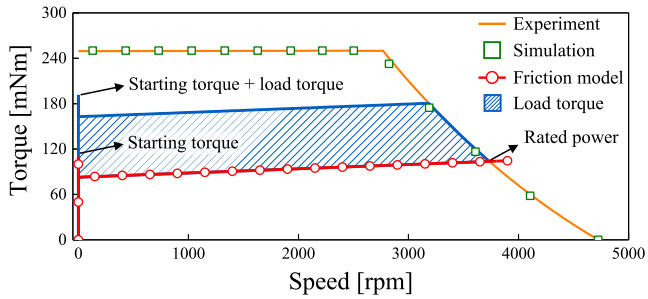

Fig. 13. Verification of the motor performance.

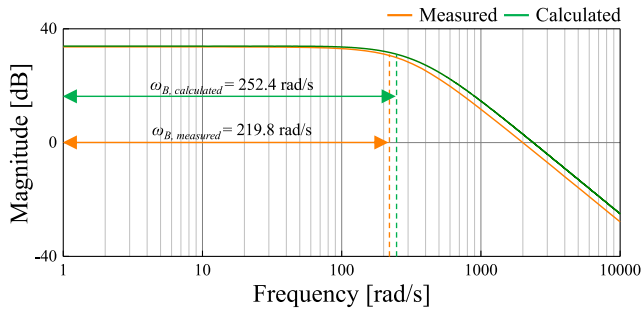

(a)

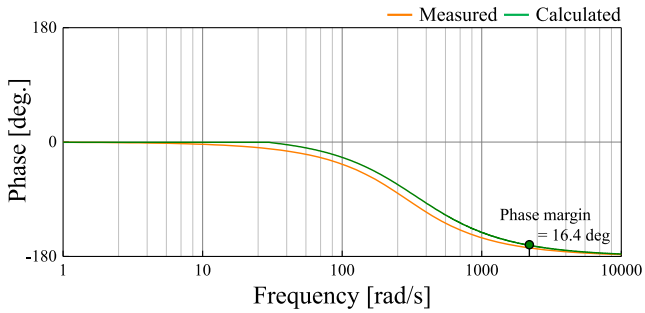

(b)

Fig. 14. Comparison of the designed motor systems frequency response. (a) Magnitude and bandwidth. (b) Phase.

TM302 torque sensor and Yokogawa WT1800 power analyzer were used in experiment to verify the simulation results. Fig. 13 shows the performance of the designed motor. The designed motor has sufficient output power to overcome the friction and load torque within the limited dc voltage.

Fig. 14(a) and (b) shows the frequency response of the designed motor system. The bandwidth using the measured parameters was 219.8 rad/s, and the bandwidth using the calculated parameters was 252.4 rad/s. The phase margin of the motor system was 16.4° at 2350 rad/s. Since the maximum speed of the motor system is 1564 rad/s as shown in Fig. 13, the motor system operates in a stable region. The electrical time constant of the designed motor system can be negligible compared with the mechanical time constant, as shown in Fig. 10(b) and (c). Thus, the bandwidth of motor system is relative low, but it is the highest bandwidth under limited conditions. Therefore, the

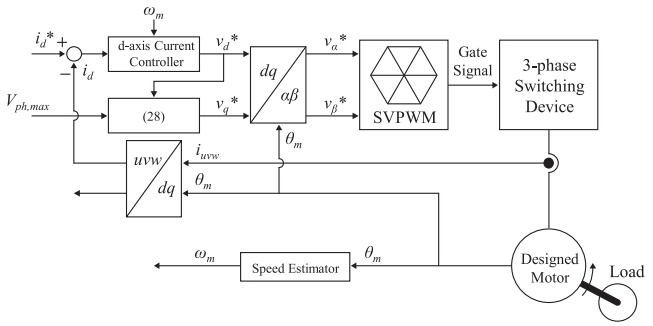

Fig. 15. Control scheme for simulation and experiment to measure the speed response of the motor system.

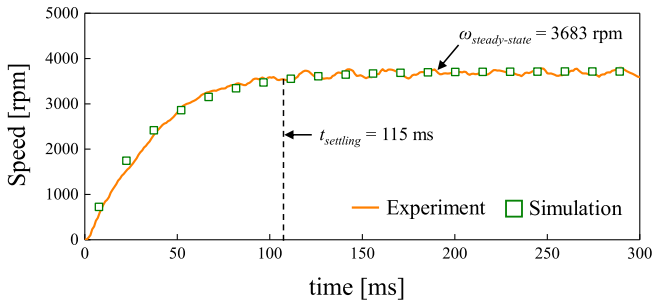

Fig. 16. Verification of the speed response.

bandwidth of the servo system can be increased when the motor system is designed by using the proposed method.

In order to derive the result of open-loop speed response, a current controller for simulation and experiment was designed in Fig. 15. A d-axis current PI controller and q-axis voltage controller are implemented. The "$i_d = 0$" control is applied in the d-axis controller to synchronize the phase of the current and back EMF. The q-axis reference voltage to maintain a constant maximum phase voltage is calculated as follows:

$$V_q^* = \sqrt{V_{\text{ph,max}}^2 - V_d^{*2}} \tag{33}$$

where V_d^* and V_q^* are the d-, q-axis reference voltage, and $V_{\text{ph,max}}$ is the maximum phase voltage. The electromagnetic system includes a three-phase switching device and the designed motor. The mechanical system includes the inertia of the motor system and the friction model of Fig. 9. To measure the speed response of the motor system to the step voltage input, the experiment set of Fig. 8(a) was used. In this experiment, the designed motor was used to operate the load instead of the servomotor. Since the speed response is constant regardless of the disturbance torque, only the experiment using the friction load was performed [17]. Fig. 16 shows the simulation and experiment results of the speed response of the motor system. The settling time of the experiment result was measured as 115 ms, 3.7 % different from the simulation result. The steady-state speed of the experiment result was the same as the rated speed 3683 r/min, which was 1.4 % different from the simulation results.

V. Conclusion and Future Works

In this article, we proposed the design methodology of the motor that can improve the dynamic speed response of the motor system. The speed response can be further improved through the motor design rather than the control technique in applications where the dynamic response is important. In the proposed method, the bandwidth of the motor system was used to evaluate the speed response. As the bandwidth is affected by electrical and mechanical time constants, the correlation of the bandwidth and time constants was investigated. The load model based on experiments was established for the determination of the required torque of the motor system and the prediction of the accurate speed response. The results showed that the designed motor system with the maximized bandwidth satisfied the rated power. Finally, the rated power of the designed motor and the speed response of the motor system were verified through simulations and experiments.

The motor system with high bandwidth can respond to a rapid disturbance torque. However, the motor generates a high torque to maintain its state when a sudden disturbance torque is applied. Since the high torque can degrade a thermal performance of the motor, the current density should be limited to maintain the thermal performance. In addition, the limited torque can lead to a result of decreasing the bandwidth of the motor system. Based on this study, the speed response of the motor system considering the thermal performance of the motor and the decrease of the bandwidth of the motor system due to the maximum torque limit will be further studied as future work. In addition, a comparative study on high- and low-bandwidth motor systems and a study on the bandwidth when the feedback current regulator is attached will be also conducted according to the switching frequency.

References

[1] S. H. Park, J. C. Park, J. M. Kim, H. Y. Lee, S. O. Kwon, and M. S. Lim, "Design of high bandwidth motor system considering electrical and mechanical time constants," in *Proc. Energy Convers. Congr. Expo.*, Sep. 2019, pp. 1308–1314.

[2] H. Gurocak, "Drive-train design," in *Industrial Motion Control*, 1st ed. New York, NY, USA: Wiley, 2016, pp. 35–106.

[3] J. R. Hendershot Jr., and T. J. E. Miller, "Basic design choices," in *Design of Brushless Permanent-Magnet Machines*, 2nd ed. Venice, FL, USA: Motor Design Books LLC, 2010, pp. 65–156.

[4] S. K. Sul, "Design of regulators for electric machines and power converters," in *Control of Electric Machine Drive Systems*, 1st ed. Hoboken, NJ, USA: Wiley, 2011, pp. 154–229.

[5] Y. Qiu, J. Sun, M. Xu, K. Lee, and F. C. Lee, "Bandwidth improvements for peak-current controlled voltage regulators," *IEEE Trans. Power Electron.*, vol. 22, no. 4, pp. 1253–1260, Jul. 2007.

[6] A. Yoo, Y. D. Yoon, S. K. Sul, M. Hisatune, S. Morimoto, and K. Ide, "Design of a current regulator with extended bandwidth for servo motor drive," in *Proc. Conf. Rec. PCC-Nagoya*, Apr. 2007, pp. 1308–1314.

[7] L. Idkhajine, E. Monmasson, and A. Maalouf, "Fully FPGA-based sensorless control for AC drive using an extended Kalman filter," *IEEE Trans. Ind. Electron.*, vol. 59, no. 10, pp. 3908–3918, Oct. 2012.

[8] L. Springob and J. Holtz, "High-bandwidth current control for torque-ripple compensation in PM synchronous machines," *IEEE Trans. Ind. Electron.*, vol. 45, no. 5, pp. 713–721, Oct. 1998.

[9] G. Lee, S. Kim, J. Hong, and J. Bahn, "Torque ripple reduction of interior permanent magnet synchronous motor using harmonic injected current," *IEEE Trans. Magn.*, vol. 44, no. 6, pp. 1582–1585, Jun. 2008.

[10] J. W. Choi and S. K. Sul, "Inverter output voltage synthesis using novel dead time compensation," *IEEE Trans. Power Electron.*, vol. 11, no. 2, pp. 221–227, Mar. 1996.
[11] H. W. Kim, M. J. Youn, K. Y. Cho, and H. S. Kim, "Nonlinearity estimation and compensation of PWM VSI for PMSM under resistance and flux linkage uncertainty," *IEEE Trans. Control Syst. Technol.*, vol. 14, no. 4, pp. 589–601, Jun. 2006.
[12] S. Morimoto, M. Sanada, and Y. Takeda, "Mechanical sensorless drives of IPMSM with online parameter identification," *IEEE Trans. Ind. Appl.*, vol. 42, no. 5, pp. 1241–1248, Sep./Oct. 2006.
[13] T. Nussbaumer, M. L. Heldwein, G. Gong, S. D. Round, and J. W. Kolar, "Comparison of prediction techniques to compensate time delays caused by digital control of a three-phase buck-type PWM rectifier system," *IEEE Trans. Ind. Electron.*, vol. 55, no. 2, pp. 791–799, Feb. 2008.
[14] M. Kim, S. K. Sul, and J. Lee, "Compensation of current measurement error for current-controlled PMSM drives," *IEEE Trans. Ind. Appl.*, vol. 50, no. 5, pp. 3365–3373, Sep./Oct. 2014.
[15] M. S. Lim, J. M. Kim, Y. S. Hwang, and J. P. Hong, "Design of an ultra-high-speed permanent-magnet motor for an electric turbocharger considering speed response characteristics," *IEEE/ASME Trans. Mechatronics*, vol. 22, no. 2, pp. 774–784, Apr. 2017.
[16] H. J. Kim, J. S. Jeong, M. H. Yoon, J. W. Moon, and J. P. Hong, "Simple size determination of permanent-magnet synchronous machines," *IEEE Trans. Ind. Electron.*, vol. 64, no. 10, pp. 7972–7983, Oct. 2017.
[17] F. Golnaraghi and B. C. Kuo, "Speed and position control of a DC motor," in *Automatic Control Systems*, 9th ed. New York, NY, USA: Wiley, 2009, pp. 289–292.
[18] M. S. Lim, S. H. Chai, J. S. Yang, and J. P. Hong, "Design and verification of 150 krpm PMSM based on experiment results of prototype," *IEEE Trans. Ind. Electron.*, vol. 62, no. 12, pp. 7827–7836, Dec. 2015.
[19] M. Nakano, H. Kometani, and M. Kawamura, "A study on eddy-current losses in rotors of surface permanent-magnet synchronous machines," *IEEE Trans. Ind. Appl.*, vol. 42, no. 2, pp. 429–435, Mar./Apr. 2006.

Soo-Hwan Park received the bachelor's degree in mechanical engineering from Hanyang University, Seoul, South Korea, in 2014, where he is currently working toward the Ph.D. degree in automotive engineering.

From 2019 to 2020, he was with the Korea Institute of Industrial Technology. His main research interests include electromagnetic field analysis, design and optimization of electric machines for automotive and robotics applications, and electric machine drive for industrial applications.

Jin-Cheol Park received the bachelor's degree in electrical engineering from Chungbuk National University, Cheongju, South Korea, in 2015, and the master's degree from Hanyang University, Seoul, South Korea, in 2017, where he is currently working toward the Ph.D. degree in automotive engineering.

His research interests include electric machine design for automotive and numerical analysis of electromagnetics.

Ho-Young Lee received the bachelor's degree in mechanical engineering from Daegu University, Daegu, South Korea, in 2012, and the master's degree in automotive engineering from Hanyang University, Seoul, South Korea, in 2014, where he is currently working toward the Ph.D. degree in automotive engineering.

He is currently a Researcher with the Korea Institute of Industrial Technology, Deagu. His research interests include design and optimization of electric machine, such as automotive application.

Soon-O Kwon received the bachelor's and master's degrees in electrical engineering from Changwon National University, Changwon, South Korea, in 2005 and 2007, respectively, and the Ph.D. degree in automotive engineering from Hanyang University, Seoul, South Korea, in 2011.

He is currently with the Korea Institute of Industrial Technology, Deagu, South Korea. His research interests include electric machine design and analysis.

Myung-Seop Lim (Member, IEEE) received the bachelor's degree in mechanical engineering and the master's and Ph.D. degrees in automotive engineering from Hanyang University, Seoul, South Korea, in 2012, 2014 and 2017, respectively.

From 2017 to 2018, he was a Research Engineer in Hyundai Mobis, Yongin, South Korea. From 2018 to 2019, he was an Assistant Professor in Yeungnam University, Daegu, South Korea, Since 2019, he has been with Hanyang University, Seoul, South Korea, where he is currently an Assistant Professor.

His research interests include electromagnetic field analysis and electric machinery for mechatronics systems such as automotive and robot applications.